Competition Between Intrinsic and Extrinsic Size Effects in Ferroelectric Thin Films with Dead Layers and Charged Point Defects

I. B. Misirlioglu*, H. N. Cologlu, M. Yildiz

Faculty of Engineering and Natural Sciences, Sabanci University, Tuzla/Orhanli, 34956 Istanbul, Turkey

---

Abstract

We analyze the effect of charged point defects on the electrical domains, phase transition characteristics and electrical properties of ferroelectric thin films with thin dead layers using a non-linear thermodynamic model. The numerical analysis takes into account various electrostatic boundary conditions, presence of thickness-wise asymmetrically distributed charged point defects as well as the elastic energy associated with the film-substrate misfit and various polarization configurations. We demonstrate that these charged defects, even when having an effective charge density less than an electron per unitcell and positioned wide apart, can pin and couple to electrical domains in films with ferroelectrically passive, so-called dead layers. Such an outcome alters the hystereses and especially the phase transition characteristics. In films that are a few nanometers thick, the spatial charge effects compete with the depolarizing field, and could lead to highly stable 180º domains accompanied by spatial pinning of polarization depending on the sign of the charge associated with the defect. It has not been clear until recently whether strong spatial variations of polarization due to charged defects could, in the absence of free charges, trigger domain formation. We find that domains do form but only when dead layers are present and not due to strong variations of polarization around defects due to their spatial fields. While relatively thick films (>14 nm in this work) with no defects could have single domain state energy close to multidomain state even when thin dead layers (~ 0.4 nm) are present, we show that charged defects locally enhance polarization, with the reservation that it might be pinned, and could enforce 180º domain formation. For films with thick dead layers (> 0.8 nm in this work), depolarizing effects dominate and the transition from the paraelectric state is into the multidomain ferroelectric state during cooling. Charged defects, on the other hand, might also override the intrinsic limit set by the dead layers in ultrathin films through their long range fields and lead to multidomains with weak, induced polarization. Ultrathin films with asymmetrically distributed charged defects have a strongly smeared ferroelectric-paraelectric transition while this effect is weaker in thicker films. The competition between defect induced extrinsic effects and the dead layer related limit is discussed.

Keywords: Ferroelectric films, charged defects, electrostatics, phase transition, thermodynamic modeling.

---

*Author to whom correspondance should be addressed: burc@sabanciuniv.edu

1. Introduction

Phenomena related to inhomogeneities and defects in ferroelectric thin films have been an interest for the scientific community for more than the last two decades. What renders defects in ferroelectric films interesting and worth studying is that the strain and field sensitivity of the permanent dipoles in a thin, planarly confined structure make dramatic changes in their configuration commensurate with strong deviations from bulk states. One fact is that the formation of defects such as ionic vacancies, interstitials and dislocation networks are inevitable owing to both the process conditions and the developing strains in the film on misfitting substrates during fabrication. The defect fields and their impact on the physical properties of ferroelectrics both in bulk and film form have been the focus of numerous studies including dedicated book chapters [1-10]. The motivation behind such effort has been understanding the structure-electrical property relation in these materials that are strong candidates for memory devices, tunable layers and antennas, pyroelectric/piezoelectric detectors as well as high-k films in integrated circuits. Furthermore, these materials have also become a test-bed in the past few decades for studying phase transitions and critical behavior in the solid state probably only second to magnetic materials.

Recently, with the emergence of techniques capable of fabricating very thin ferroelectric films on misfitting substrates, wherein the distances through which defect fields permeate become comparable to film thickness, related effects have gained a special importance. Various degradation mechanisms were attributed to defects that create frozen-in electric fields as well as local strain fields that are demonstrated to be long-ranged [8, 10-16]. In addition to being held responsible for degradation, defects with charges near the surfaces have also been treated as centers strongly influencing switching characteristics or hinder domain wall motion [9, 18, 19]. Lately, misfit dislocations with extended strain fields have been the focus of many groups both by experimental and theoretical means [8, 11, 15-18, 19]. These line defects distort the lattice in their vicinity, giving rise to position dependence of properties, also well documented experimentally [8, 20]. A similar situation arises in the presence of a localized and partially screened charges of any source: A charged defect can directly create electrostatic fields strong enough to modify the dipole configuration in its surrounding. Just as important, one must also consider the type of mechanisms by which the defect fields couple to the ferroelectric lattice. For instance, a misfit dislocation with a full unit cell length Burgers vector parallel to the substrate-film interface creates compressive and tensile strains at short distances the latter of which stabilizes a dominantly in-plane polarization (P) inside the film when the half plane is inside the substrate. The field of the charged defect, on the other hand, will strongly depend on its location with respect to the film-electrode interfaces in a capacitor structure as well as the electrostatic boundary conditions.

When attempting to compute the macroscopic effect of a network of defects, the combined effect of strain-polarization coupling in addition to electric field-polarization coupling could become a complex problem. Thus, also from an experimental point of view, it could become quite difficult to distinguish different contributions to observed properties. An example to the latter is the discussions on whether the disappearance of ferroelectricity in ultrathin films is an intrinsic behavior set by atomistic mechanisms or caused by interfacial inhomogeneities and imperfections that put an extrinsic limit on the film thickness capable of sustaining desired functionality. With theoretical studies on the stability of ferroelectricity on substrates subject to various electrical boundary conditions in addition to quantum mechanical first principles calculations, there is now consensus that the intrinsic size limit to ferroelectricity is a result of competing energies involving atomic mechanisms, relaxation of electrostatic energy and boundary conditions, strain and electrical domain formation [20-31]. However, how such an intrinsic limit trend, particularly in the light of the electrostatic considerations at the interfaces, would be modified in the presence of even a low density of charged defects remains a very interesting question. Furthermore, charged point defect effects in ferroelectric thin films have often been qualitatively discussed and assessed but quantitative studies have been scarce.

In this article, in order to address the question as to whether or not intrinsic and extrinsic size effects could compete in thin ferroelectric films, we study the behavior of ferroelectric thin films with charged defects sandwiched between metallic electrodes with dead layers. To probe the strength of the charged defect effects we use the Landau-Ginzburg-Devonshire (LGD) formalism for ferroelectric materials coupled with the interface conditions and defect fields. We observe that charged defect effects can prevail in terms of stabilizing a weak, induced ferroelectricity even at relatively far distances from defect sites via an imprinted P in ultrathin films with dead layers not thicker than a few unit cells. Defects also stabilize and pin electrical domains in films around or a little thicker than 14 nm. This is not because of the strong spatial variations of P around them but via the overall enhancement throughout the film thickness commensurate with an enhancement in the depolarizing field emanating at the film-dead layer interface. Possible large values of the dielectric constant of the dead layer (a few hundred or more) is certainly expected to impact the domain stabilities in ultrathin films but does not pose an interesting case within the current context.

For relatively thick films (>20 nm) with a few defects, the behavior does not change compared to perfect films despite both having dead layers and is kept outside the current content. Also checking for the stabilization of electrical domains as well as rotation of *P* inside the film, we find that there is a non-negligible in-plane *P* in the vicinity of the defects despite misfit strain states favoring out-of-plane *P* in addition to the rotation of *P* near domain-domain-dead layer intersections. As defect type, we choose to work with charged lattice defects that are introduced into the system as point potentials whose values can be assigned. The appropriate electrostatic boundary conditions, which are agreed upon by nearly all research groups in the field, are taken into account as well as the elastic strain energy due to the film-substrate misfit that couple to the components of ferroelectric polarization. We also account for the non-linear terms of the in-plane *P* and its cross-terms with the out-of-plane *P* until the sixth power term in the LGD energy and associated gradient energies to account for the full coupling of the charged defects to all components of *P*.

Following the simulation of *P* at room temperature (RT) subject to the aforementioned film-electrode interface conditions, we study the RT hystereses and temperature variation of *P*. While the hystereses are slightly displaced and distorted along the electric field axes in the presence of defects with charge, an important observation in our simulations is that a low concentration of charged lattice defects, even in the presence of a dead layer, can pin the *P* as well as the 180° domains at not too-strong applied bias in ultrathin films with thickness close to those where either size driven ferroelectric-paraelectric transitions or transition into a multidomain state are reported to occur [21, 23]. Moreover, we find that at thicknesses where we obtain zero solution for the P in perfect films with thin dead layers, defects can render finite P values comparable to a fraction of bulk values in the form of domains even away from defect sites, implying the long range impact of defects in ultrathin films. In the latter case, defects act as sources of field that couple to the rest of the film through the electrodes in spite of the dead layers. In the absence of an applied field, the electrical domains form in a way that the defect field is parallel to the P in the local domain. There also exists a region in the close vicinity of the defects that does not switch with applied field or that requires fields higher than the coercive values of the defect-free film. Such an occurence would mean that high densities of charge trapping or electrostatically imbalanced defects would cause serious loss of switchable P in ultrathin films together with a highly stable multidomain structure when dead layers are present.

2. Methodology

In order to study the effect of charged lattice defects at a local and global level, we first form a two dimensional grid that is $200n$ x kn cells where k (200) is the number of cells along the film thickness (width) and each cell, n, has a dimension of 0.4 nm, imitating the unit cell dimensions of well known perovskites such as PZT and BT. This way, the order of lengths at which P can vary in the system is closest to real systems. To find polarization, we solve the equations of state derived from the LGD free energy for all P in our system for an epitaxial monodomain (001) ferroelectric film on a (001) cubic substrate coupled with the Maxwell equation for dielectric displacement employing a finite difference discretization. The total volumetric free energy of the system is:

$$F_T = \int_V \left[w(F_0 + F_P + F_E + F_G - F_{ES}) + (1-w)F_{DL} \right] dV \qquad (1)$$

where w is a step-wise function defining the interface between the dead layer and the ferroelectric in the following manner:

$$w=1 \text{ when } -h/2 \le z \le +h/2$$

$$w=0 \text{ when } -h/2-s < z < -h/2 \text{ and } +h/2 < z < s+h/2, \qquad (2)$$

and s is the dead layer thickness, h is the thickness of the ferroelectric layer. The electrode-dead layer interfaces are at $-h/2-s$ and $s+h/2$ respectively. F_0 is the energy of the paraelectric state and

$$\begin{aligned} F_P &= \alpha_1 (P_1^2 + P_2^2 + P_3^2) + \alpha_{11}(P_1^4 + P_2^4 + P_3^4) + \alpha_{12}(P_1^2 P_2^2 + P_1^2 P_3^2 + P_2^2 P_3^2) \\ &\quad + \alpha_{111}(P_1^6 + P_2^6 + P_3^6) + \alpha_{112}[P_1^4(P_2^2 + P_3^2) + P_2^4(P_1^2 + P_3^2) + P_z^4(P_1^2 + P_2^2)] \\ &\quad + \alpha_{123} P_1^2 P_2^2 P_3^2 \end{aligned} \qquad (3)$$

is the energy due to the polarization P_i (i=1,2,3) in the ferroelectric state, and α_i, α_{ij}, and α_{ijk} are the dielectric stiffness coefficients (Compiled from Ref. 32). F_E in Eq. (1) is the internal elastic energy both due to the misfit between the film and the substrate as well as the self-strain given by:

$$F_E = \frac{1}{2} C_{ijkl} \left(\varepsilon_{ij} - \varepsilon_{ij}^0 \right) \left(\varepsilon_{kl} - \varepsilon_{kl}^0 \right) \qquad (4)$$

where the C_{ijkl} are the elastic stiffnesses for a cubic crystal, $\varepsilon_{11}=\varepsilon_{22}$ and is the film-substrate misfit strain in the pseudocubic limit along *x* and *y*, ε_{ij}^{0} is the self-strain energy due to the paraelectric-ferroelectric phase transition in the film and is given by:

$$\varepsilon_{ij}^{0}=\begin{pmatrix} Q_{11}P_1^2+Q_{12}(P_2^2+P_3^2) & Q_{44}P_1P_2 & Q_{44}P_1P_3 \\ Q_{44}P_1P_2 & Q_{11}P_2^2+Q_{12}(P_1^2+P_2^2) & Q_{44}P_2P_3 \\ Q_{44}P_1P_3 & Q_{44}P_2P_3 & Q_{11}P_3^2+Q_{12}(P_1^2+P_2^2) \end{pmatrix} \quad (5)$$

with Q_{ij} being the electrostrictive coefficients for a cubic crystal in the contracted notation. The shear components of stress in (4) are taken as zero due to the traction-free film surface. The in-plane biaxial misfit state with equal orthogonal components due to epitaxy require that $P_1=P_2$, and the rest of the equations are given hereafter accordingly. The magnitude of the elastic energy is determined by the misfit as well as the *P* stability along *x* and *z*. The gradient energy in Eq. (1) is given by:

$$\begin{aligned} F_G &= G_{33}\left(\frac{dP_3}{dz}\right)^2+G_{31}\left(\frac{dP_3}{dx}\right)^2+G_{13}\left(\frac{dP_1}{dz}\right)^2 \\ &+G_{11}\left(\frac{dP_1}{dx}\right)^2+G_{23}\left(\frac{dP_2}{dz}\right)^2+G_{21}\left(\frac{dP_2}{dx}\right)^2 \end{aligned} \quad (6)$$

where G_{ij} are the gradient energy coefficients. For thin layers or inhomogeneous structures, the gradient energy has a significant effect on *P* and determines the domain morphologies. In our calculations, we shall assume that the gradient energy is isotropic for convenience, and thus $G_{33}=G_{31}=G_{13}=G_{11}=G_{23}=G_{21}=G$. We also neglect the variations along P_2 along *y* within the two dimensional limit of this work. F_{ES} is the electrostatic energy of the system whose energy scales with the magnitudes of the applied potential and gradients of *P* as well as the polarizability of the dead layer as explained in the coming paragraphs. F_{DL} is simply the energy of the dead layer that is assumed to be a linear dielectric and is given by:

$$F_{DL} = \varepsilon_0 \varepsilon_r (E_x^2 + E_z^2) \tag{7}$$

with E_X and E_Z being the electric field components along the x and z axes that are computed from the Maxwell relations described in the forthcoming paragraphs, ε_r is the dielectric constant of the dead layer and is assumed to be isotropic for convenience. Minimization of Eqn. (1) for w=1 yields the following Euler-Lagrange relations:

$$\begin{gathered}\frac{dF_T}{dP_3} - \frac{d}{dz}\left(\frac{dF_T}{df_1}\right) - \frac{d}{dx}\left(\frac{dF_T}{df_2}\right) = 0, \\ \frac{dF_T}{dP_1} - \frac{d}{dz}\left(\frac{dF_T}{df_3}\right) - \frac{d}{dx}\left(\frac{dF_T}{df_4}\right) = 0\end{gathered} \tag{8}$$

with $f_1 = dP_3/dz$, $f_2 = dP_3/dx$, $f_3 = dP_1/dz$ and $f_4 = dP_1/dx$. From Eqns.(8) and (1), the equations of state for the ferroelectric layer are written as:

$$\begin{aligned} G\left(\frac{d^2P_3}{dz^2} + \frac{d^2P_3}{dx^2}\right) &= 2\alpha_3^m P_3 + 4\alpha_{13}^m P_3 P_1^2 + 4\alpha_{33}^m P_3^3 + 6\alpha_{111} P_3^5 \\ &\quad + \alpha_{112}(4P_3P_1^4 + 8P_3^3P_1^2) + 2\alpha_{123} P_3 P_1^4 - E_Z \end{aligned} \tag{9a}$$

$$\begin{aligned} G\left(\frac{d^2P_1}{dz^2} + \frac{d^2P_1}{dx^2}\right) &= 2\alpha_1^m P_1 + 2(2\alpha_{11}^m + \alpha_{12}^m)P_1^3 + 2\alpha_{13}^m P_1 P_3^2 + 6\alpha_{111} P_1^5 \\ &\quad + 2\alpha_{112}[3P_1^5 + 3P_1^3P_3^2 + P_1P_3^4] + 2\alpha_{123} P_1^3 P_3^2 - E_X \end{aligned} \tag{9b}$$

in the ferroelectric film where the α_3^m, α_{13}^m, α_{33}^m are the renormalized dielectric stiffness coefficients, modified by the misfit strain, the electrostatic field, and the two-dimensional clamping of the film [33]. The dead layer, when present, is assumed to be a high-k dielectric whose dielectric constant, ε_r, is 20 to exemplify its effects. The electric fields in the above equations are computed from the gradient of the electrostatic potential ϕ,

$$E_Z = -\frac{d\phi}{dz},\ E_x = -\frac{d\phi}{dx} \tag{10}$$

The electrostatic potential is found at each point in the system using the Maxwell relation in the absence of free charges,

$$\nabla \cdot D = 0 \tag{11}$$

where $D_Z = \varepsilon_b \varepsilon_0 E_Z + P_3$ and $D_X = \varepsilon_b \varepsilon_0 E_X + P_1$ in our two dimensional case with ε_b being the background dielectric constant (taken as 10 in this work) and the fields can be inserted into (11) with their forms given in (10). Equations (10) and (11) relate the strength of the depolarizing electric field to the variations in the components of *P* both in the film as well as the ferroelectric-dead layer interface. The boundary conditions we employed for $P_{1,3}$ are

$$\frac{dP_1}{dx} = 0 \text{ and } \frac{dP_3}{dz} = 0 \tag{12}$$

at the top and bottom electrode-film interface of the ferroelectric layer corresponding to an infinite extrapolation length, λ, and periodic boundary conditions are used along the sides (*x*-axis), i. e.,

$$P_3(z, x=0) = P_3(z, x=L),\ P_1(z, x=0) = P_1(z, x=L) \tag{13}$$

Dirichlet boundary conditions are applied at the dead layer-electrode interfaces, *-h/2-s* and *s+h/2*, to solve the fields coupled with $P_{1,3}$ components where $\phi = 0$ at both top and bottom dead layer-electrode interfaces correspond to total charge compensation while periodic boundaries are adopted along *x* as given in (13). It is important to remind here that the charge compensation is at the dead layer-electrode interfaces, meaning that bound charges are partially screened at the ferroelectric-dead layer interfaces depending on the dead layer thickness.

Equations (9) – (11) are solved simultaneously employing a Gauss-Seidel iterative scheme subject to boundary conditions mentioned above. The simulations always start with small fluctuations of z and x components of P components around zero that later on develop into the domain structure depending on dead layer and film thickness. We limit ourselves to 5000 iterations converging to a difference of 10^{-8} between consecutive iterative P solution steps when ferroelectricity exists. We also benefited from a relaxational tool that weighs and considers the local values of ϕ with respect to nearest and next nearest neighbors in our iterative runs to avoid difficulties arising from possible abrupt variations in P components coupling to electric potential via (11) in the initial stages of the iterations that can otherwise lead to diverging solutions.

To get the electric field dependent behavior of the films, we simply change ϕ on one of the electrodes and keep the other at zero and thus the film sees an electric field. A triangular signal for ϕ is used to get the hystereses of the films with maximum voltage drop amplitudes chosen depending on the film thickness. The signal consists of 100 steps between -2V and +2V. At every incremental bias step, we allow the films to reach their near-equilibrium P configuration. Hence, the hystereses in our simulations are in the quasi static limit. The charged defects are assumed to be of the type that does not distort the local lattice and only creates an electric field in the surrounding vicinity coupled with the electrostatic boundary conditions. They are introduced as fixed local point potentials, imitating a semi-screened uncompensated charge complex near the film-electrode interfaces that contribute to the total potential in the system at every cell through their

Coulomb fields that are solved automatically using (9) and (10) while finding ϕ. Therefore, the total field in (9) contain the defect fields, too, when they are present.

The paraelectric-ferroelectric phase transition characteristics are studied through finding P_3 by varying temperature between RT and 900ºC. These simulations are run for films that are 6.4 and 14.4 nm thick in the presence and absence of charged defects. At each temperature, the equations given above are solved for all P components and the resulting configuration constitued the initial condition for the next step. The thickness of the dead layers in these runs are also specified when necessary to demonstrate the competition between defect effects and the dead layer effects.

The material system considered in this study is heteroepitaxial (001) PZT 30/70 fully strained on a (001) $SrTiO_3$ (ST) substrate with pseudomorphic top and bottom metallic electrodes. The values of the dielectric stiffness coefficients and other thermodynamic parameters entering the calculations are given in Table I and are taken from Ref. 32. Simulation results are presented for PZT 30/70 films of 6.4 nm, 14.4 nm thickness.

3. Results and Discussion

3.1 Room temperature domain structures

We start by discussing the stable domain structures of the films at RT for various film/dead layer thickness with and without defects in the light of our results obtained using the methodology prescribed. A representative schematic for the system considered is given in Figure 1. The dead layer thicknesses are chosen as either one or two unit cells in all cases with a fixed dielectric constant value of 20. The defects, when present, are placed as point potentials within the discretization scheme of this work with a value of 1V at half a unit-cell distance away from the charge source, imitating a partially screened vacancy site with a ~2x10^{-21} C effective charge in a unit cell with symmetric fields. For convenience, they are placed at the bottom dead layer-ferroelectric interface with equal seperation having a value of 40 nm to be able to check the long-range effects of individual defects. Note that configuration of defects can easily be changed and random positions at the interface can be assigned. Thus we focus on a low density of defects with asymmetric interface. One must, of course, come to realize that a large density of randomly distributed charged defects would dramatically alter the properties within the context of our approach. However, for the sake of clarity and keeping the focus intact, we avoid examining the extreme cases that could also easily be done otherwise.

In Figure 2a-b, the colormap comparison between the P_3 configurations at RT for 6.4 nm thick films with one unitcell thick dead layers are given in the presence and absence of interface defects after 5000 iterations for full coherence on (001) ST. In the 6.4 nm thick films, the 180º domains form regardless of the presence of defects as long as a dead layer exists at the electrode-film interfaces (Figure 2a-b). One can easily note that the domain period in the film with defects is larger. We obtain the domain period for the defect-free 6.4 nm film as 13.33 nm whereas this is 16 nm for the defected film. This is due to the enhancement of P_3 in the vicinity of the defects in which the order of distances that this enhancement takes place is comparable to the film thickness, favoring a positive P_3 with the rest of the film coupling to these fields via the electrodes. However, we have to also state here that the relation between the domain period and defect strength as well as defect density is not straightforward to evaluate and requires a systematic study which will be undertaken in another study. For example point defect complexes with very strong bias fields enforce a P_3 matching the sign of the defect field accompanied by a stronger depolarizing field and a more complicated, a rather irregular domain pattern could develop in regions away from defects, especially when defect period is random near the interfaces. In the defected 6.4 nm film, it is worthy to note that the domains form in a way wherein the domain aligns with the defect being fixed in the center. Thus the domains develop in a way so as to be energetically compatible with these defect fields.

The results for the effect of defects on the stability of 180º domains in the 6.4 nm film under bias are given in Figure 2c-d both for $\varepsilon_r = 20$. A voltage of -0.2 V is applied to the bottom electrode while the upper electrode is kept at 0 V. We chose -0.2 V as this is sufficient to induce small but noticable effects of bias in films considered here in the thermodynamic limit. In the presence of the bias, there is not a very notable change in the film with no defects: After 5000 iterations under the mentioned bias, the film sustains the domain structure with a slightly higher number of switched cells in favor of the bias field. When defects are present, defect fields enhance the P_3 in the vicinity of and this conversely impacts the number of sites that have switched. As seen in Figure 2d, there is a significant portion that have not switched but the behavior is still comparable to that of the defect-free 6.4 nm film. On the other hand, the domain period, in both films remains nearly constant under -0.2 V bias. An applied field opposing the sign of the defect induced field has to have values higher than those for a defect-free film to induce complete switching. Moreover regardless of whether defects are absent or not, a remnancy of P_3 in the hysteresis is not observed as will be shown in the next section, owing to multidomain stability.

In Figure 3a-b we provide the results for the 14.4 nm thick films with two unit cell dead layers (s=2). We study the 14.4 nm thick films with dead layers thicker than that for the 6.4 nm films as we noticed that there is a proximity of the energies of the single domain state and multidomain states, creating a possibility of convergence to metastable or unstable solutions that do not pose an interesting case. For s=2 unit cells, the domains are stable in the defect-free film and a multidomain state persists when charged defects are present at the bottom interface (Figure 3a-b) at zero bias. The domain period for the defect free film is interestingly larger than that of the defected film, where the former has 20 nm period and the latter has 16 nm. This is just the opposite of what has been obtained for the 6.4 nm film. We note that the defected film also has a slightly larger $\left|P_3\right|$ in each domain along the midsection of the 14.4 nm film owing to a defect bias (See Figure 3c). The decrease in the domain period of the 14.4 nm film is both due to the fact that domains want to configure themselves in favor of the defect fields as well as a slightly stronger depolarizing field emanating from the defect-bias-enhanced P coupling to the rest of the film volume. After the zero-field simulations, to understand how domains will adapt, we next discuss the effect of a small applied bias field during the simulations forcing the P_3 to switch in the next paragraph.

In the 14.4 nm thick film, upon applying a -0.2 V bias to the bottom electrode, it is seen that, while the defect-free film has nearly switched (See Figure 4a), electrical domains persist in the defected one (See Figure 4b). The near-single domain state under -0.2 V bias in the defect-free 14.4 nm film is related to fact that the depolarizing field is weaker. In contrast, the film with defects has strongly pinned domains, both due to defect fields and the commensurately larger depolarizing fields as well. The pinning we are discussing here is purely of electrostatic origin where defect fields influence the regions away from the defect sites via electrodes. Such an effect is strong enough to make cells away from the defect sites to a certain extent resist switching. It is critical here to notice that the depolarizing field magnitude will change with variations in the P_3 throughout the film while the defect fields are fixed. Defect induced fields sustain the multidomain configuration owing to the enhancement of P_3 in the domains through the long-range effects despite the -0.2V bias on the system acting to weaken the defect induced fields.

Recalling the results for the 6.4 nm film, one can say that the 14.4 nm film is under the influence of an enhanced depolarizing field with respect to the defect-free one due to the bias induced by defects instead of a strong thickness-driven depolarizing effect pronounced the 6.4 nm one. A profound enhancement of the local bias fields of defects in ultrathin films is due to steeper potential drops at shorter distances creates a strong competition between these defect fields and the depolarizing field. The former is impacting a significant film volume in terms of favoring a P of a matching orientation. Therefore, the domain period in the 6.4 nm film with defects is larger than that of the defect-free film while an opposite trend is observed for the 14.4 nm film.

A critical aspect we observed in our simulations is discussed in this paragraph with a focus on the plot in Figure 5. This is a good example to solely demonstrate the existence of a ferroelectric state with small but finite P having a relatively diffuse multidomain configuration in the presence of defects. The ultrathin film has a thickness of 4.8 nm with one unit cell thick dead layers having $\varepsilon_r = 20$. When no charged defects are present, we find P_3 at each cell around $\pm 10^{-26}$ after 5000 iterations, meaning literally zero P_3 within the numerical limits of this work. The small but finite P_3 with electrical domains away from the defect sites despite the 40 nm spacing between these defects is a clear indication of possible long-range impact of charged complexes in ultrathin films. This domain structure forms through the defect induced potentials creating fields in the majority of the film whose interface bound charges are screened through dead layers. Note that the domains with - P_3 exist, away from the defect sites, an indirect effect of the defect bias fields coupling to the defect-free regions via the electrodes. However, a remnant P_3 in the latter is not observed: There is just a nonlinear variation of P_3 with applied bias. Films with s=1 and thinner than ~ 4.8 nm exhibit only an induced P_3 just near the defect sites and is paraelectric when defects are not present. For the sake of completeness, Figure 5b is provided to show that very thin films (3.2 nm in this case) will exhibit only locally induced P with either very weak or no coupling to the defect-free sites in the presence of a unit cell thick dead layers.

3.2 Hysteresis simulations

We proceed with the extraction of the quasi-static hysteresis loops ($<P_3>$-V plots) to observe the effect of charged defects at the film-dead layer interfaces at RT. In Figure 6 we give our results for $<P_3>$ vs. applied bias in 6.4 nm films with dead layers in the absence and presence of defects. The dead layer is two unit cells thick with its relative dielectric constant being 20 as usual. A zero-remnancy hystereses behavior is observed in the 6.4 nm film, due to the stability of the domain structure at low-to-mid values of applied field in the thermodynamic limit. Thus, what just happens is a domain wall motion in proportion to applied field. In the presence of defects, the hysteresis loop becomes somewhat deformed and slightly rotated and displaced along the P_3 axis (Figure 6a). Note that the defected film will probably have also a slightly lower dielectric permittivity than the defect-free film at small bias due to the small slope difference, dP/dE, near zero bias. In general, the 6.4 nm film with $s=1$ does not exhibit any remnancy regardless of whether defects are present or not. The stability of multidomains results from a strong depolarizing field that dominates and dictates the electrical response of the system to any applied signal.

In Figure 6b, we focus on the hysteresis loops of the 14.4 nm thick film with two unit cell thick dead layers. In the case of $s=1$, we see a square hysteresis (Figure 6b). The defect-free 14.4 nm thick film with two unitcell thick dead layers displays a double loop hysteresis with a nearly zero remnant P_3, owing to an effective depolarizing field smaller but comparable to the 6.4 nm thick film. Figure 7, on the other hand reveals that the 14.4 nm thick film's double loops begin to separate with a linear section in the middle when defects are present compared to the defect free 14.4 nm film. This is a direct indication of the pinned electrical domains at low bias in the film with charged defects where a non-linear response of $\langle P_3 \rangle$ to the applied bias is possible after around $|0.12|$ V in both directions. Also note that there is also a slight asymmetry in the left and right portions of the loop. A linear P-V curve at low bias, as in the case of the film with defects mentioned above, points to a limited motion of domain walls. As much as domain pinning can be perceived as a detrimental process in some applications, we would like to remind that it could also be beneficial in applications where a relatively high-*k* but no hysteretic behavior is desired.

3.3 Phase transition characteristics

In this section, we provide our results where the polarization states in the 6.4 nm and 14.4 nm thick films are computed as a function of temperature in the presence and absence of defects. Before we go onto discussing the competition between the intrinsic-extrinsic limit effects, we take the *P*-*T* curve for perfect 6.4 nm and 14.4 nm films with no dead layers as reference as shown in Figure 8. The P_3 solutions and T_C of the two cases is the same and is around 880ºC, near twice the bulk T_C due to the compressive in-plane misfit. When present, dead layers at both electrode-film interfaces are assumed to exist at a thickness of one unit cell as already mentioned in the 6.4 nm film. We choose so as dead layers that are two unit cell thick reduce the T_C dramatically, to about 80ºC, (not shown here) confining the transition to a small *T* region with respect to thicker films. During the simulations, if the transition from the paraelectric state is into a multidomain ferroelectric state, one can track $<\left|P_3\right|>$ to allow the detection of the transition point in our simulations or else a bias with the intention of stabilizing a single domain state at T_C could substantially modify the phase transition characteristics of the systems, especially in the 6.4 nm films. Note that a non-zero $<|P_3|>$ solution indicates ferroelectricity in the films.

Figure 9a shows the $<P_3>$ and $<|P_3|>$ in the 6.4 nm thick film without and with defects respectively. The transition temperature for the defect free film is around 150ºC.

The film with charged interface defects have a strongly smeared transition [34] in the 150-300ºC range with a non-zero $<P_3>$ remaining and gradually leveling off at elevated temperatures. The depolarizing field, when dead layers are present, is quite strong for the 6.4 nm film due to the bound charge induced potential drop at shorter distances when electrodes are kept at zero potential. Therefore, T_C is lowered significantly in the defect-free 6.4 nm film. A multidomain structure with the majority of the volume having a positive P_3 in favor of the defect fields is stable at low temperatures (Please see the $<P_3>$ for the defected films in Figure 9a). We remind again here that these films are also under the influence of a size limit via the depolarizing field taking effect in the presence of dead layers. The strong smearing originating from defect fields when they are present, however, does not allow us to strictly comment on the shift in the transition temperature. But the defect fields apparently enhance the overall P_3 in the film as seen from Figure 9a despite dead layer effects.

The charged defects in the 14.4 nm thick film have a different impact on P_3 throughout the temperature range of interest in this study as shown in Figure 9b. The paraelectric-ferroelectric transition temperature for the defect-free 14.4 nm film is around 500ºC and into a multidomain state during cooling. Moreover, in the presence of the defects, a smearing is also observed but weaker than the case of the 6.4 nm film. Throughout the whole temperature range, there is a non-zero, positive P_3 when defects are present that implies the presence of a built-in P_3. Similar results have been recently obtained for thick (200 nm) single domain PZT 30/70 that does not have any dead layers but high densities of continuous space charge distribution near one of the electrodes [35]. A stronger smearing in the 6.4 nm film is resulting from the fact that the defect fields are much more effective due the film thickness, causing steeper potential drops that induce larger electric fields. Note that we can only judge the extent of the smearing of the transition due to defects via tracking $<|P_3|>$ or else the net order state of the system is difficult to observe.

4. Conclusions

We have demonstrated the general characteristics of the effect of charged point defects on domain formation and phase transition characteristics of ferroelectric thin films using the (001) PZT 30/70 on (001) ST system as an example. The competition between the defect induced electrostatic fields with the depolarizing fields due to dead layers is most prominent in the ultrathin films. Frozen-in defect fields, even when corresponding to local, effective charge densities less than an electron/unit cell volume, could strongly pin the domains in ultrathin films by electrostatic means, reducing the switchable P_3 as well as slightly deforming the hysteresis shapes. Owing to the thickness effects, the competition between the defect fields and the depolarizing field is more pronounced in the ultrathin films, pinning the local P_3 in a stronger fashion. We again would like to remind here that the pinning here is purely of electrostatic origin and is a consequence of the defect field that actually scales with film thickness. Such an electrostatic pinning mostly impacts the average remnant P_3 and does not have an apparent contribution so as to increase the thermodynamic coercive field.

As shown in this study, the 14.4 nm thick film turns out to have better beneficial properties as well as a potentially more stable P_3 when dead layers are thin and it seems that thicker films are likely to be under a less significant influence of defects with electrical fields. Therefore, low densities of not-very strong charged defects appears to be tolerable in sufficiently thicker films (>14 nm for the PZT 30/70 on ST system in this study). We conclude so by noting the energetics of the single domain and multidomain states in the 14.4 nm film with thin dead layers. This is also due to the larger distances along the film thickness where the potential drops will occur compared to ultrathin films, weakening the defect effects as long as the dead layers are not thicker than a unit cell or less. Clearly, this will not be so if the film has a lower T_C (not far from RT) either due to in-plane strain or due to relatively thick dead layers. In addition, the consequences of such processes might be hard to precisely predict and high defect densities might impact single domain stability in real systems.

Domain periods are influenced from defect fields in an exactly opposite fashion in the 6.4 and 14.4 nm thick films within the limits of dead layer thicknesses triggering domain formation. Defect fields in ultrathin films have a larger domain of influence while weaker defect fields in the 14.4 nm film mostly lead to an overall enhancement of $|P_3|$ accompanied by a growing density of bound charges at the film-dead layer interface. Along with defect site-domain compatibility, a slight enchancement in the P_3 jump at the film-dead layer interface leads to a smaller period multidomain sequence. Therefore, the dead layers play a significant role in the domain-defect coupling, particularly in the case of interface-wise asymmetrically situated defects. A film with a perfect film-electrode interface but still having charged defects will exhibit asymmetrically displaced loops mostly along the field axis. We also showed that widely seperated charged defects whose strengths are less than that of an electron charge, with seperation distances several times the film thickness, can render existence of ferroelectricity feasible in ultrathin films, capable of overriding the intrinsic size effect due to dead layers in ultrathin films. This happens in the form of multidomains, revealing the long range coupling of defect fields to dipoles far away from the defects, altering the limit of the paraelectric state. Such an effect, maybe not so beneficial for applications requiring a switchable *P*, might exhibit itself in structural characterization studies by a slight tetragonality as well as an asymmetric dielectric response with respect to bias in a typical capacitance-voltage measurement.

During near-equilibrium cooling, the paraelectric-ferroelectric transition is much more strongly smeared in ultrathin films (<7 nm in this study) compared to thicker ones (> 14 nm in this study) even in the presence of widely seperated charged defect sites that have accumulated on one side of the film along the film plane. The depolarizing effects compete with defect fields in ultrathin films as demonstrated wherein the reduction in T_C is significant in films in this work regardless of the presence of defects. It is obvious that charged defects, when high in density, can very significantly alter the properties but the depolarizing fields also develop accordingly, dictating the electrical response as well as the domain configuration for films with dead layers. In summary, the competition between the dead layer induced intrinsic limit of ferroelectric stability and the defect induced effects will be much more pronounced with decreasing film thickness.

Acknowledgements

The authors gratefully acknowledge Sabancı University for software and hardware support.

References

1. S. Triebwasser, Phys. Rev. **118**, 100 (1960).
2. A. P. Levanyuk and A. S. Sigov, "*Defects and Structural Phase Transitions*", Volume 6, in *Ferroelectricity and Related Phenomena*, edited by W. Taylor, Gordon and Breach Science Publishers, (1988).
3. W. L. Warren, D. Dimos, G. E. Pike, B. A. Tuttle, M. V. Raymond, R. Ramesh and J. T. Evans, Appl. Phys. Lett. **67**, 866 (1995).
4. T. M. Shaw, S. Troiler-McKinstry, P. C, Mcintyre, Ann. Rev. Mat. Sci. **30**, 263 (2000).
5. R. Ramesh, S. Aggarwal and O. Auciello, Mat. Sci. Eng. Rep. **32**, 191 (2001).
6. C. S. Ganpule, A. L. Roytburd, V. Nagarajan, B. K. Hill, S. B. Ogale, E. D. Williams, R. Ramesh and J. F. Scott, Phys. Rev. B **65**, 014101 (2002).
7. H. Z. Jin and J. Zhu, J. Appl. Phys. **92**, 4594 (2002).
8. M.-W. Chu, I. Szafraniak, R. Scholz, C. Harnagea, D. Hesse, M. Alexe and U. Gösele, Nat. Mater. **3**, 87 (2004).
9. X. Ren, Nat. Mater. **3**, 91 (2004).
10. (9.5) E. Cockayne and B. P. Burton, Phys. Rev. B, **69**, 144116 (2004).
11. D. Balzar, P. A. Ramakrishnan and A. M. Hermann, Phys. Rev. B **70**, 092103 (2004).
12. S. P. Alpay, I. B. Misirlioglu, V. Nagarajan, R. Ramesh, Appl. Phys. Lett. **85**, 2044 (2004).
13. Y. Xiao, V. B. Shenoy and K. Bhattacharya, Phys. Rev. Lett. **95**, 247603 (2005).

14. W. Laguta , A. M. Slipenyuk, I. P. Bykov, M. D. Glinchuk, M. Maglione, D. Michau, J. Rosa, and L. Jastrabik, Appl. Phys. Lett. **87**, 022903 (2005).
15. Y. Zheng, B. Wang and C. H. Woo, Appl. Phys. Lett. **88**, 092903 (2006).
16. I. B. Misirlioglu, Mark Aindow, S. P. Alpay, and V. Nagarajan, Appl. Phys. Lett. **88**, 102906 (2006).
17. Y. L. Li, S. Y. Hu, S. Choudhury, M. I. Baskes, A. Saxena, T. Lookman, Q. X. Jia, D. G. Schlom and L. Q. Chen, J. Appl. Phys. **104**, 104110 (2008).
18. S. V. Kalinin, S. Jesse, B. J. Rodriguez, Y. H. Chu, R. Ramesh, E. A. Eliseev and A. N. Morozovska, Phys. Rev. Lett. **100**, 155703 (2008).
19. D. Schrade, B.X. Xu, R.Muller and D. Gross, Proc. Appl. Math. Mech. **7**, 4040015 (2007).
20. C. L. Jia, S. B. Mi, K. Urban, I. Vrejoiu, M. Alexe and D. Hesse, Phys. Rev. Lett. **102**, 117601 (2009).
21. J. Junquero and P. Ghosez, Nature **422**, 506 (2003).
22. Z. Q. Wu, N. D. Huang, Z. R. Liu, J. Wu, W. H. Duan, B. L. Gu and X. W. Zhang, Phys. Rev. B **70**, 104108 (2004).
23. D. J. Kim, J. Y. Jo, Y. S. Kim, Y. J. Chang, J. S. Lee, J. G. Yoon, T. K. Song and T. W. Noh, Phys. Rev. Lett. **85**, 237602 (2005).
24. J. M. Wesselinowa, S. Trimper and K. Zabrocki, J. Phys. Cond. Mat. **17**, 4687 (2005).
25. G. Gerra, A. K. Tagantsev, N. Setter and K. Parlinski, Phys. Rev. Lett. **96**, 107603 (2006).
26. A. M. Bratkovsky and A. P. Levanyuk, Ferroelectrics **359**, 1 (2007).

27. R. Ahluwalia and D. J. Srolovitz, Phys. Rev. B **76**, 174121 (2007).

28. J. Paul, T. Nishimatsu, Y. Kawazoe and U. V. Waghmare, Phys. Rev. Lett. **99**, 077601 (2007).

29. M. Stengel, D. Vanderbilt and N. A. Spaldin, Nat. Mater. **8**, 392 (2009).

30. A. M. Bratkovsky and A. P. Levanyuk, Phil. Mag. **90**, 113 (2010).

31. E. Almahmoud, I. Kornev and L. Bellaiche, Phys. Rev. B **81**, 064105 (2010).

32. M. J. Haun, Z. Q. Zhuang, E. Furman, S. J. Jang, L. E. Cross, Ferroelectrics **99**, 45 (1989).

33. See “N. A. Pertsev, A. G. Zembilgotov and A. K. Tagantsev, Phys. Rev. Lett. **80**, 1988 (1998)” for how these normalized coefficients are obtained.

34. A. M. Bratkovsky and A. P. Levanyuk, Phys. Rev. Lett. **94**, 107601 (2005).

35. I. B. Misirlioglu, M. B. Okatan and S. P. Alpay, J. Appl. Phys.**108**, 034105 (2010).

Figure Captions

Figure 1. (Color Online) The schematic of the ferroelectric capacitor considered in this study and the reference coordinates for the P components.

Figure 2. (Color Online) The RT domain configurations of the 6.4 nm thick film with dead layers and $\varepsilon_r = 20$ for (a) defect-free film, (b) the film with charged defects near the bottom electrode, (c) defect-free film under -0.2V bias (d) film with defects under -0.2V bias. Scales are given to display the range of P_3 in C/m^2.

Figure 3. (Color Online) The RT domain configurations of the 14.4 nm thick film with dead layer dielectric constant 20 for (a) defect-free film, (b) the film with charged defects near the bottom electrode, (c) the value of P along the white, dashed midline of the defect-free and defected film given in (a) and (b). Scales are given to display the range of P_3 in C/m^2.

Figure 4. (Color Online) The domains in the 14.4 nm film under -0.2 bias for , (c) defect-free film and (d) film with defects. Scales are given to display the range of P_3 in C/m^2.

Figure 5. (Color Online) (a) The defect-induced weak multidomain structure in the 4.8 nm thick film with one unit cell thick dead layers. (b) Defects in a 3.2 nm thick film. Scales are given to display the range of P_3 in C/m^2.

Figure 6. (Color Online) Hysteresis loops for (a) the defect-free 6.4 nm film, (b) the defect-free 14.4 nm thick film for s=1 and s=2.

Figure 7. (Color Online) Hysteresis loop for the 14.4 nm thick film with charged defects at the bottom film-dead layer interface.

Figure 8. (Color Online) *P*-*T* curve for the 14.4 and 6.4 nm thick films without any defects or dead layers. There is perfect overlap and therefore the results are exactly the same for the two thicknesses. Open circles: 14.4 nm thick film, small red solid circles: 6.4 nm thick film.

Figure 9. *P*-*T* curves for (a) the defect-free and defected 6.4 nm thick film and (b) defect-free and defected 14.4 nm thick film. Squares: $<|P_3|>$ for defect-free film, open circles: $<|P_3|>$ for defected film, solid small circles: $<P_3>$ for defect-free film, triangles: $<P_3>$ for defected film in both (a) and (b)

Table I. Thermodynamic parameters, free energy coefficients, electromechanical and elastic coefficients of PZT 30/70 used in this study, compiled from Ref. 32.

Parameter/Constant	**PZT 30/70**
T_C (ºC, bulk)	440
ε_0 (10^{-12} F/m)	8.85
C (ºC)	$1.5\text{x}10^5$
α_{11} (10^7 m^5/C^{2}F)	0.6458
α_{111} (10^8 m^9/C^{4}F)	2.348
α_{12} (10^8 m^5/C^{2}F)	5.109
α_{112} (10^8 m^9/C^{4}F)	10.25
α_{123} (10^8 m^9/C^{4}F)	-5.003
S_{11} (10^{-12} Pa^{-1})	8.4
S_{12} (10^{-12} Pa^{-1})	-1.7
S_{44} (10^{-12} Pa^{-1})	9.24
Q_{11} (10^{-2} m^4/C^2)	7.887
Q_{12} (10^{-2} m^4/C^2)	-2.480
Q_{44} (10^{-2} m^4/C^2)	6.356
D_{33}, D_{13}, D_{23} (10^{-10} m^3/F)	5.0
λ (m)	infinite
u_m at RT	-0.0166

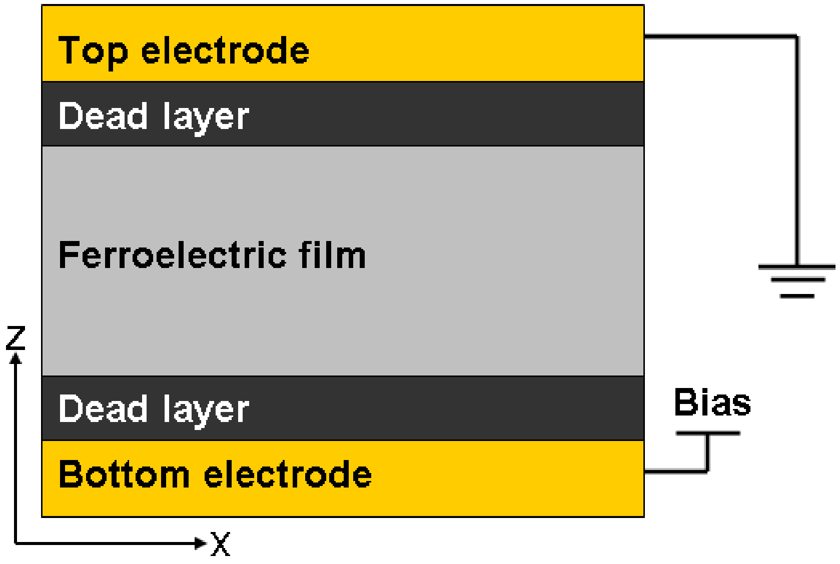

Figure 1. Misirlioglu *et al.*

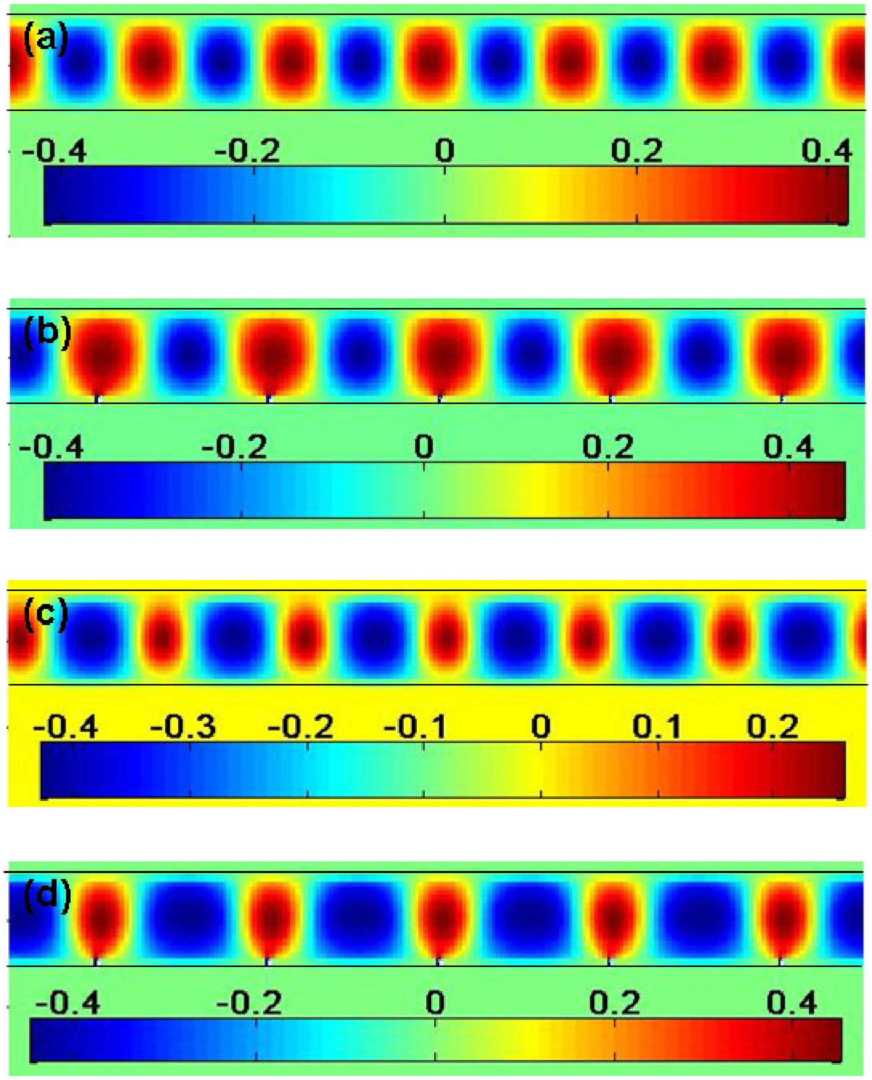

Figure 2. Misirlioglu *et al.*

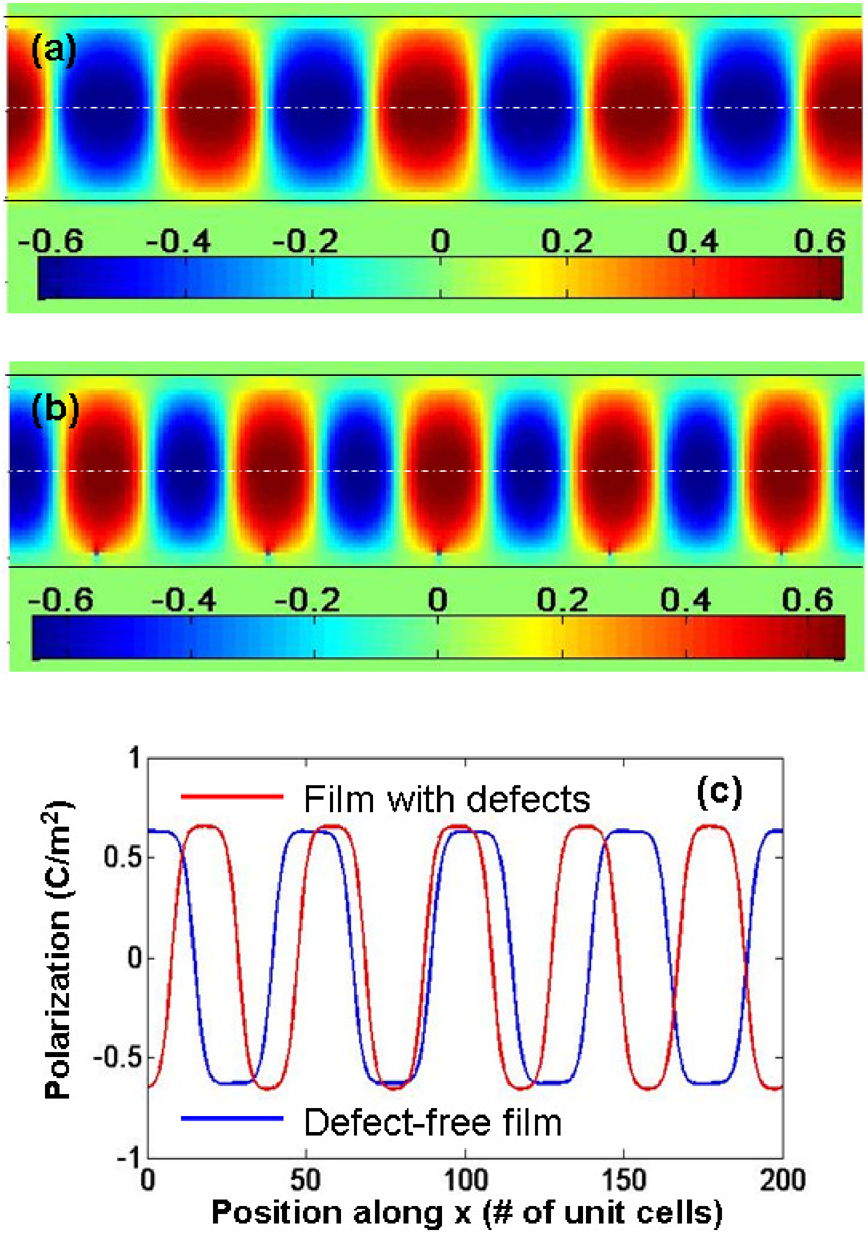

Figure 3. Misirlioglu *et al.*

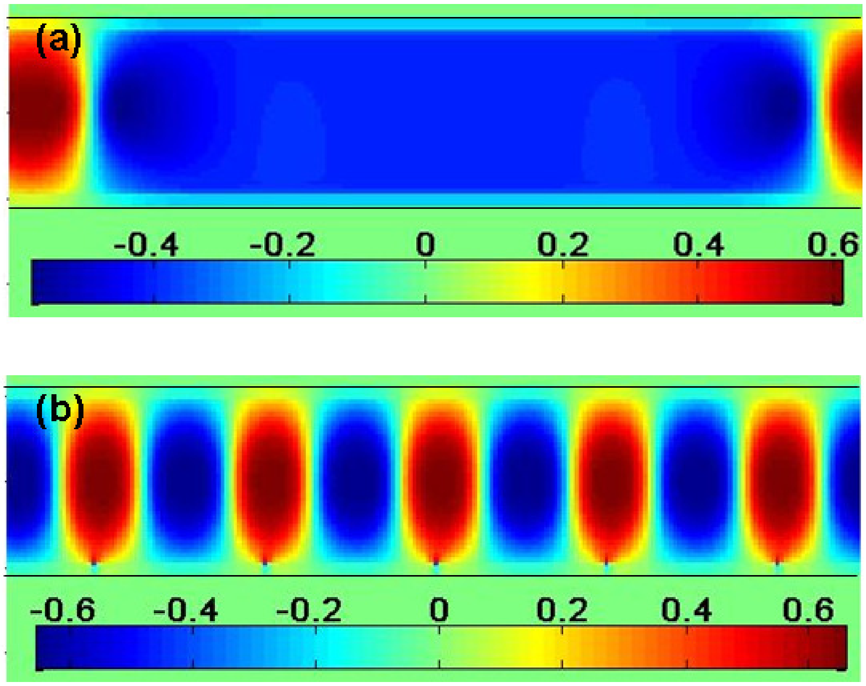

Figure 4. Misirlioglu *et al.*

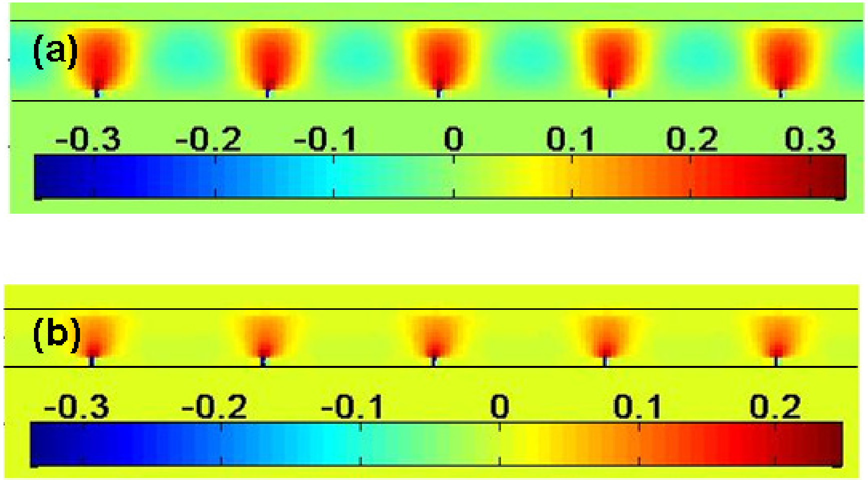

Figure 5. Misirlioglu *et al.*

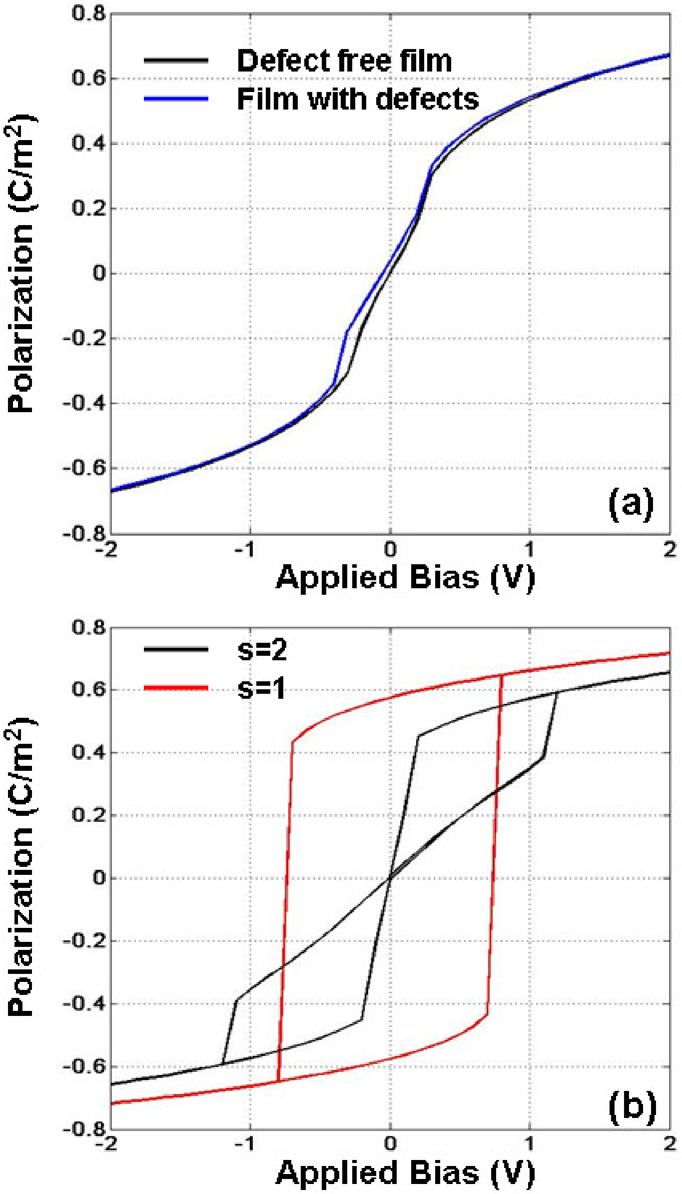

Figure 6. Misirlioglu *et al.*

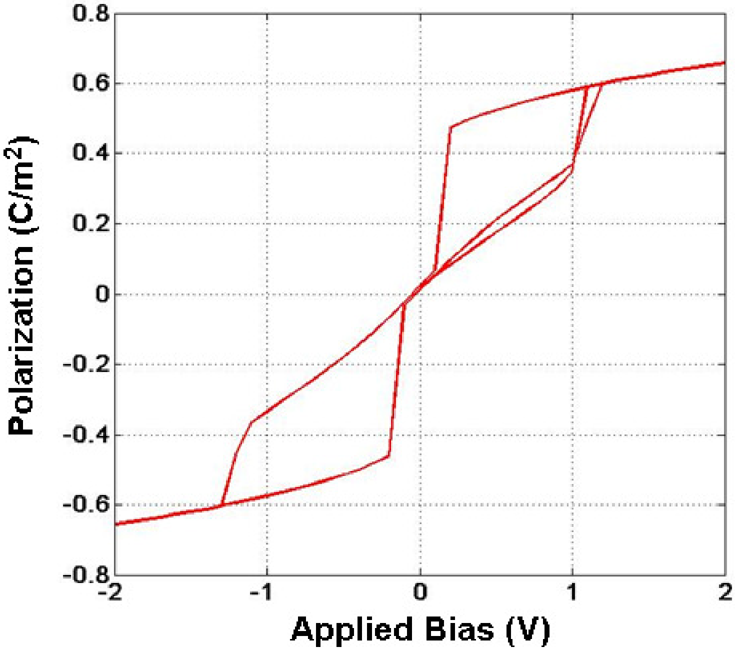

Figure 7. Misirlioglu *et al.*

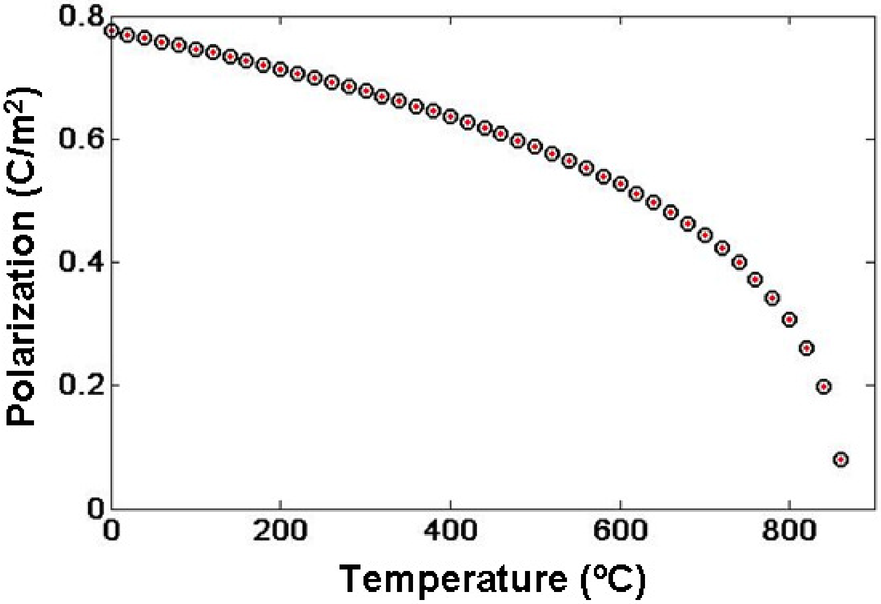

Figure 8. Misirlioglu *et al.*

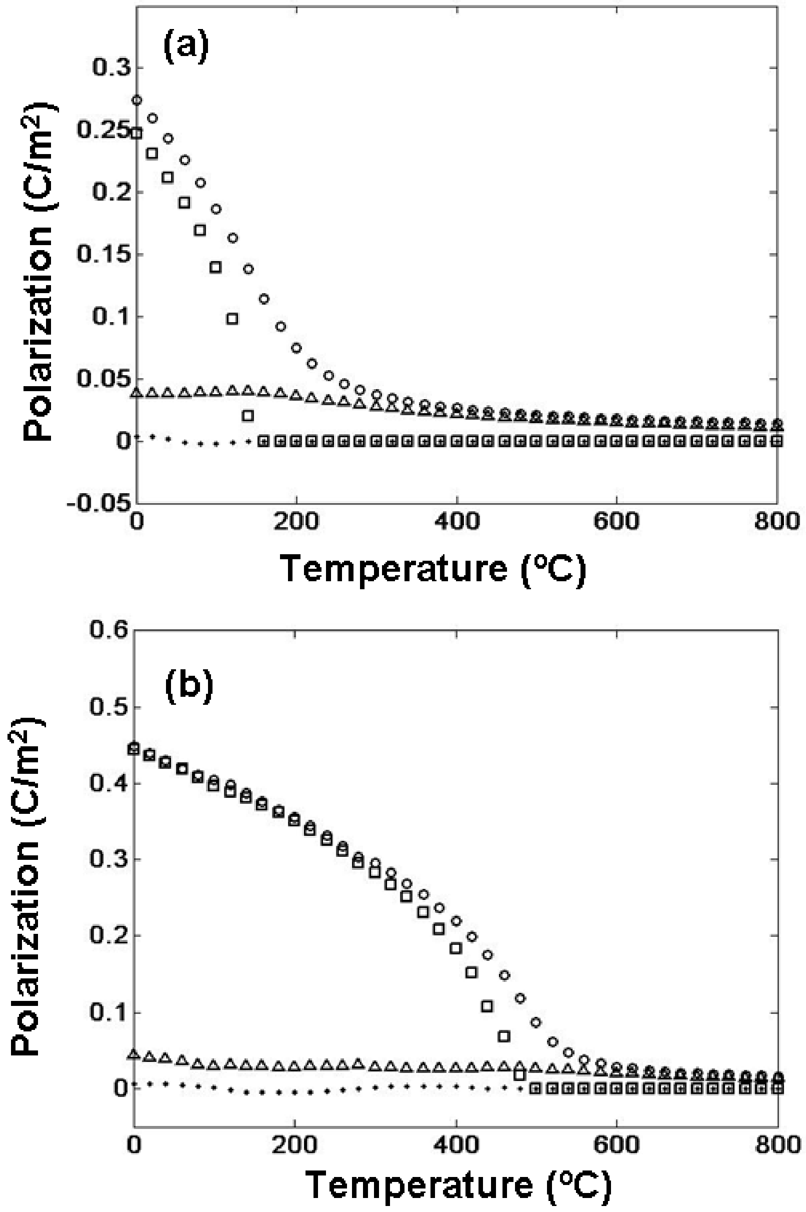

Figure 9. Misirlioglu *et al.*